

Development of a nonhuman primate computational phantom for radiation dosimetry

Tianwu Xie^{a)}

Institute of Radiation Medicine, Fudan University, 2094 Xietu Road, Shanghai 200032, China

Department of Medical Imaging and Information Sciences, Geneva University Hospital, Geneva, Switzerland

Jin Seo Park

Department of Anatomy, Dongguk University School of Medicine, Gyeongju, Korea

Weihai Zhuo

Institute of Radiation Medicine, Fudan University, 2094 Xietu Road, Shanghai 200032, China

Habib Zaidi

Department of Medical Imaging and Information Sciences, Geneva University Hospital, Geneva, Switzerland

Geneva Neuroscience Center, Geneva University, Geneva, Switzerland

Department of Nuclear Medicine and Molecular Imaging, University of Groningen University Medical Center Groningen, Groningen, Netherlands

Department of Nuclear Medicine, University of Southern Denmark, DK-500, Odense, Denmark

(Received 24 June 2019; revised 1 November 2019; accepted for publication 13 November 2019; published 29 December 2019)

Purpose: The nonhuman primate (NHP) is an important animal model for evaluating the response of the human body to radiation exposure owing to similarities between its organ structure, genome, life span, and metabolism. However, there is a lack of radiation dosimetry estimations for NHPs. The aim of this work is to construct a computational phantom of NHPs and estimate absorbed fractions and specific absorbed fractions for internal radiation dosimetry.

Materials and methods: A female rhesus monkey was frozen and sectioned using a cryomacrotome. The transaxial sectioned images were imported into Adobe Photoshop for segmentation of internal organs. A total of 31 organs/tissues were identified and labeled. The segmented voxel phantom was then converted to a boundary representation (BREP) phantom to enable easy alteration of the phantom to mimic monkeys of different stature. The BREP model was then voxelized and imported into the MCNPX Monte Carlo radiation transport code for electron and photon dosimetry calculations. To estimate the appropriateness of using human phantoms as surrogate models for NHPs, absorbed fractions (AFs) and specific absorbed fractions (SAFs) of monoenergetic electrons and photons were calculated and compared with the ICRP reference newborn female phantom and a 1-yr-old female phantom.

Results: Considerable differences were observed for both self-absorbed and cross-absorbed doses for some organs between the NHP phantom and newborn phantom. For example, the ratios of the self-absorbed $\text{SAF}_{(\text{stomach wall}) \text{ Monkey}}$ to $\text{SAF}_{(\text{stomach wall}) \text{ Newborn}}$ ranged from 0.06 at 10 keV to 0.29 at 3 MeV for photons while the corresponding ratios to cross-absorbed $\text{SAF}_{(\text{liver} \rightarrow \text{kidney}) \text{ Monkey}}$ to $\text{SAF}_{(\text{liver} \rightarrow \text{kidney}) \text{ Newborn}}$ ranged from 0.78 at 50 keV to 5.78 at 10 keV for photons. Conversely, values of self-absorbed SAF were much higher (ratios of 2.39–4.19) for the brain and much lower for the uterus (0.51–0.61) in the monkey model compared to the newborn phantom. These dose differences can be attributed to the disparities between organ masses, shapes, and positions between the two phantoms.

Conclusions: The developed NHP model can be exploited for the assessment of radiation dose to NHPs in preclinical radiation dosimetry studies and radiation therapy research. © 2019 American Association of Physicists in Medicine [<https://doi.org/10.1002/mp.13936>]

Key words: computational model, Monte Carlo simulations, nonhuman primates, radiation dosimetry

1. INTRODUCTION

Laboratory animals are widely used as models of human disease in preclinical research for the development and testing of new treatment strategies and imaging methods.¹ The animal models are also used to investigate the radiation dose

exposure–response relationship. Commonly used laboratory animals include the mouse, rat, ferret, rabbit, pig, canine, and nonhuman primates (NHPs).² Research performed with NHPs is likely to be more fruitful since their organs structure, genome, life span, and metabolism are closer to humans than other species. Accordingly, NHPs, such as

rhesus macacus and macaca fascicularis, are important animal models to mimic radiation effects on the human body.³ Radiation therapy research and acute radiation syndrome (ARS) studies with NHP subjects are widespread owing to the similarities of dose–response relationships between humans and NHPs.^{4–6}

To reach the full potential of ARS studies, multimodality imaging, radiation therapy, and radiotracer development research using NHPs, suitable computational models, and radiation dosimetry data must be made available to the research community. At present, there is a lack of realistic computational models and radiation dose estimates for NHPs to enable the calculation of absorbed doses in preclinical research studies.^{7,8} As such, human models were commonly used to perform dosimetry calculations.^{9–12} Therefore, there is a need for such models and detailed dose estimates to fill a gap in the radiation dosimetry literature.

The aim of this work was to construct the first realistic NHP computational model and generate an exhaustive radiation dosimetry database for monoenergetic photons and electrons for subsequent preclinical studies on NHPs involving dose assessment for radiobiology studies of ARS, novel molecular imaging probes, or testing radiation therapy approaches. Both voxel- and boundary representation (BREP) surface-based representations were used to describe the internal organ structures and total body surface of the developed NHP computational phantom. The BREP phantom is represented by a polygon mesh or nonuniform rational B-splines (NURBS) to combine the advantages of stylized- and voxel-based modeling in terms of anatomical realism, scalability, and flexibility. The calculated radiation doses for the NHP phantom were compared with those of the ICRP reference newborn phantom with similar weight¹³ and the RADAR 1-yr-old human phantom¹⁴ with close body length.

2. MATERIALS AND METHODS

2.A. Acquisition of monkey image dataset

Image acquisition was performed at Dongguk University School of Medicine in Korea on an 8-yr-old female rhesus monkey of 75.8 cm length and 4.3 kg where MRI, CT, and cryosection images were collected.¹⁵ The digital cryosection images were obtained at 8688×5792 image resolution, corresponding to a pixel size of $0.024 \text{ mm} \times 0.024 \text{ mm}$ and were then downsampled to intervals and pixel resolution of $0.1 \text{ mm} \times 0.1 \text{ mm} \times 0.1 \text{ mm}$ for image segmentation. Figure 1 shows the obtained CT, MRI, and cryosection images of the rhesus monkey at the level of the head, chest, and abdomen.

2.B. Image segmentation and construction of the BREP model

Image segmentation was performed manually on color cryosection images by identifying organs and tissues of

interest to produce the voxelized phantom. The boundaries between organs and tissues were manually contoured using Adobe Photoshop®. The whole process took about 2 months under the guidance of the atlas of the monkey anatomy.¹⁵ Each segmented region was labeled with a number referring to a particular organ or tissue (Fig. 1). A total of 31 organs were identified while non-identified regions, such as muscles, connective tissues, blood vessels, and adipose tissues, were assigned to a single region referred to as residual tissues.

Polygon-mesh model was constructed by using the marching cubes algorithm and the visualization toolkit (VTK)¹⁶ where the segmented contours of the voxel model were extracted and reconstructed as conformal organ surfaces and outer body contour. Following three-dimensional (3D) reconstruction, the polygon-mesh model was imported into Rhinoceros® where smooth NURBS surfaces were fitted to these polygon-mesh representations of organs and tissues. First, contours were extracted from each polygon-mesh organ model. Thereafter, a cubic NURBS surface is lofted through the contours to define starting and ending points. BREP models of the small intestine (SI) and large intestine (LI) were recreated using pipe models following the central trace of the intestine. The central trace of the pipe for the small intestine covering the reconstructed intestine region was manually created while the central trace of the large intestine was obtained from the cryosections. The thicknesses of the intestinal walls were determined through measurements performed on the images and were uniform along the whole organ. The complex bone sites, such as the skull, pelvis, and feet, were described by using the polygon-mesh geometry to keep the structure details. BREP models cannot be straightforwardly used as input to most standard Monte Carlo simulation tools. Therefore, the constructed NHP BREP model was voxelized at a resolution of $2.0 \text{ mm} \times 2.0 \text{ mm} \times 2.0 \text{ mm}$ using an in-house developed C++ code for voxelization.

2.C. Monte Carlo simulations

The extensively benchmarked MCNPX multiparticle Monte Carlo radiation transport code¹⁷ was adopted for the simulation of particle transport of monoenergetic photons and electrons in the developed NHP model. Photon and electron sources were assumed to be uniformly distributed throughout 31 segmented source regions while monoenergetic particles were generated from the source with energy grids ranging from 0.01 to 3.0 MeV for photons and 0.1 to 3.0 MeV for electrons, respectively. In the absence of well-established characteristics of NHPs, the tissue density and chemical compositions of the NHP model were assumed to be similar to those recommended for humans. Therefore, the tissue density and element compositions of human organs and biological tissues were obtained from ICRP publication 89.¹⁸ Photons were fully transported while a cutoff energy of 10 keV was set for secondary electrons to speed up the simulations without compromising the accuracy of energy deposition calculations. Particle histories were set at 1.0×10^7 particles per source organ at each energy for both photons

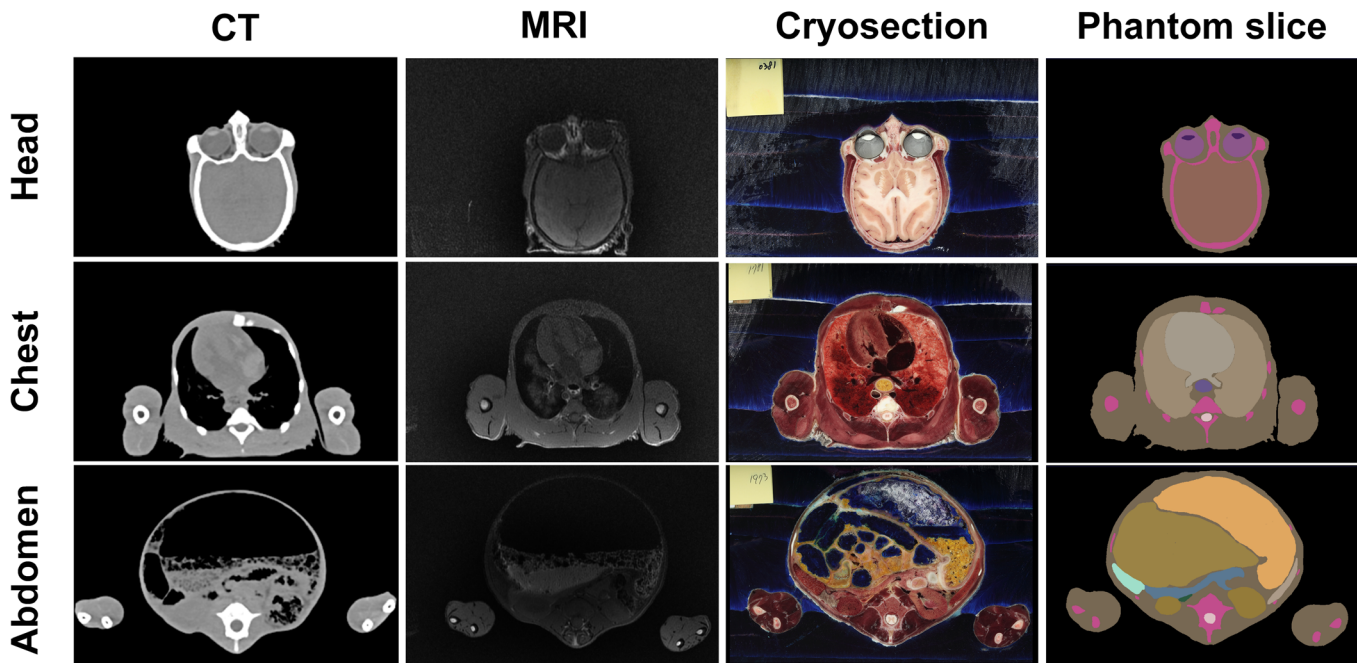


FIG. 1. Representative slices of computed tomography, magnetic resonance imaging, and cryosection images along with the segmented voxelized rhesus monkey phantom at the level of the head, chest, and abdomen [Color figure can be viewed at wileyonlinelibrary.com]

and electrons. The energy deposition in source and target organs was recorded in MeV. Table I summarizes Monte Carlo simulation details according to the report of the AAPM Task Group 268.¹⁹

2.D. Radiation dose calculations

According to the formalism recommended by the medical internal radiation dose (MIRD) committee, the absorbed dose D to target organ r_t from internal sources r_s can be calculated as²⁰:

$$D(r_t) = \sum_{r_s} S(r_s \rightarrow r_t) A(r_s) \quad (1)$$

$$\begin{aligned} S(r_s \rightarrow r_t) &= \frac{1}{M(r_t)} \sum_i E_i Y_i \varphi(r_s \rightarrow r_t, E_i) \\ &= \sum_i E_i Y_i \Phi(r_s \rightarrow r_t, E_i) \end{aligned} \quad (2)$$

where $S(r_s \rightarrow r_t)$ refers to the S-value which describes the mean absorbed dose to the target region per unit of nuclear transition in the considered source region. E_i and Y_i are initial energy and the yield of emitted radiation per nuclear transformation in the source region. $M(r_t)$ is the mass of the target organ. φ is the absorbed fraction (AF) which describes the fraction of energy absorbed in the target organ from radioactivity present in the source and can be calculated as the quotient of deposited energy divided by E_i . Φ refers to the specific absorbed fraction (SAF), which presents the absorbed fraction in the target organ per unit mass of the target organ. AF, SAF, and S-values are common dosimetric quantities used for the calculation of the absorbed dose in the human body and laboratory animals. The values of the AF and SAF depend on radiation type, energy, and the mass and shape of the target organ. The S-value depends on the decay scheme of the radionuclide, the energy, type, and yield of radiation per nuclear transformation, and the mass

TABLE I. Monte Carlo simulation details

Item name	Description	References
Code	MCNPX V2.4.0	[17]
Validation	The Monte Carlo code was previously validated for internal radiation dosimetry (for monoenergetic photons and electrons, positron-emitting radionuclides, and radiopharmaceuticals)	
Source description	Particle type: uniformly distributed monoenergetic photons and electrons in 31 segmented source regions	
Cross sections	Cross sections are generated using the libraries MCPLIB02 and EL03 for photon and electron transport, respectively	
Transport parameters	The default transport parameters of MCNPX were used	[17]
VRT or AEIT	The energy cutoff for photon and electron are 1 keV	
Scored quantities	The Monte Carlo scored quantity is deposited energy [in MeV] in each organ per number of starting photons and electrons.	
Number of histories	1.00E + 07	
Postprocessing	The postprocessing for the present study is described in the following section	

and shape of the target organ within the computational phantom.

Prior to the development of the NHP phantom described in this work, human models were used as an approximation for the assessment of radiation doses to NHP models from studies involving the use of radiopharmaceuticals to obtain the pharmacokinetics and estimate the absorbed dose in the human body.^{9–12} Total body weight is the most commonly used matching criteria for substitute phantom selection while

the torso length or standing height can be used as secondary criteria.²¹ The weight of the ICRP reference newborn phantom is 3.5 kg (81% of the mass of the NHP phantom) while the body length of the 1-yr-old human phantom is 76.8 cm (1 cm longer than the NHP phantom). To explore the appropriateness of using human phantoms as surrogate models for NHPs, we compared the absorbed doses of the newborn phantom and the 1-yr-old pediatric phantoms to the NHP phantom.

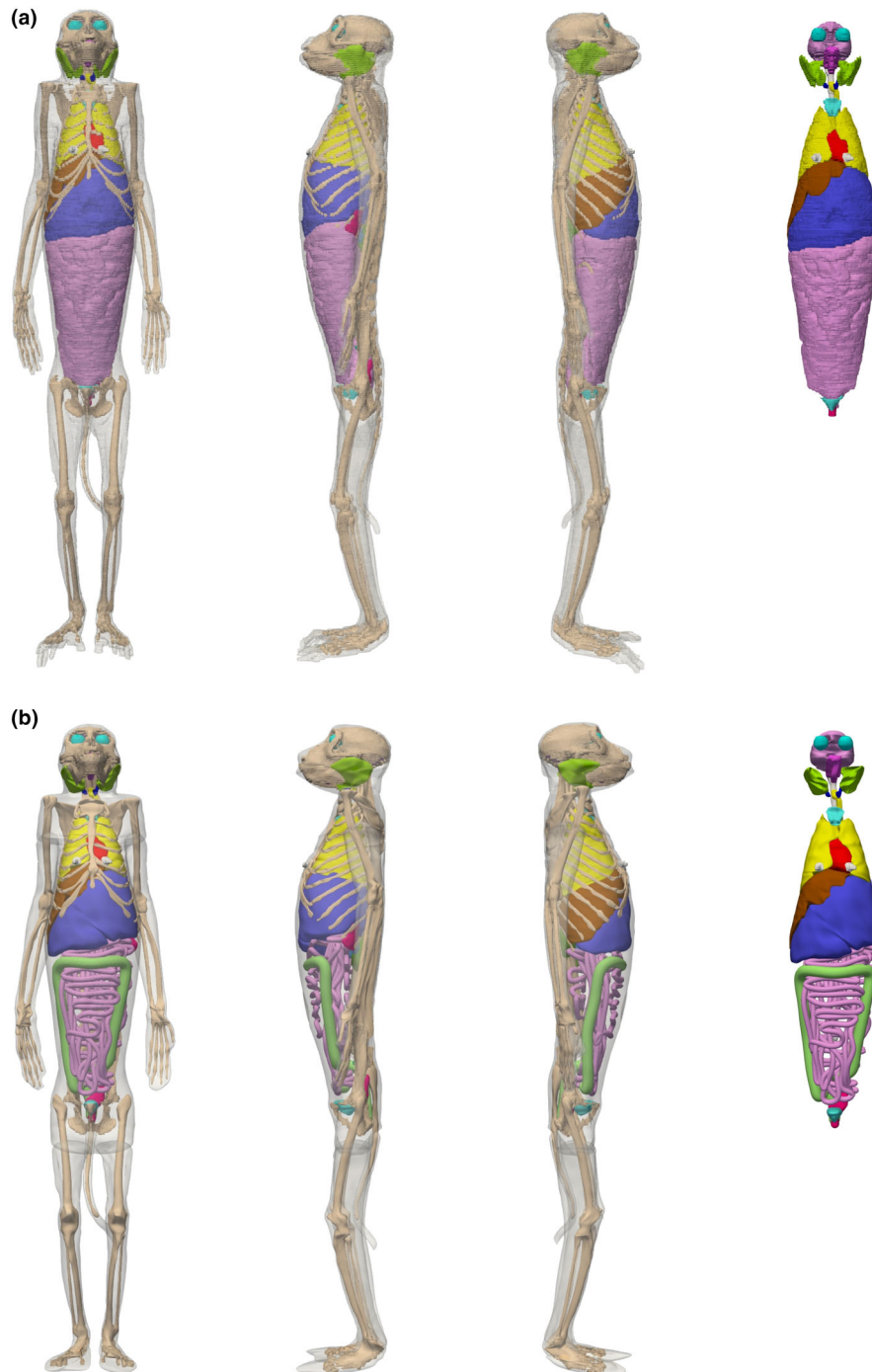


FIG. 2. Three-dimensional visualization of different versions of the nonhuman primate computational phantom: (a) Voxel-based model and (b) nonuniform rational B-splines surface model generated using Rhinoceros software [Color figure can be viewed at wileyonlinelibrary.com]

The obtained AF and SAF of monoenergetic photons and electrons can be further adopted to calculate S-values of radionuclides according to Eq. (2). Iodine-131 has been used for the therapy of differentiated thyroid cancer since 1943²² and is still one of the most widely used radionuclides in clinical trials molecular radiotherapy. In preclinical studies, NHP subjects were used to evaluate the *in vivo* biodistribution and radiation safety of ¹³¹I-labeled radiotracers.²³ S-values for Iodine-131 were therefore calculated using the decay data obtained from the radiation dose assessment resource (RADAR).²⁴

3. RESULTS

3.A. Computational NHP phantom

Figure 2 shows 3D visualizations of the segmented voxel model and constructed BREP model. The final organ masses were calculated by multiplying the density and organ volumes of the voxelized version of the BREP-based NHP phantom (Table II). The total body mass of the constructed NHP phantom was 4.3 kg. The NHP organ masses were compared with those of the ICRP reference newborn. The ratios of organ masses for the gall bladder, liver, lung, eyeballs, pancreas, and thyroid gland between the NHP and newborn are close to the total body weight ratio while the masses of adrenal glands, brain, kidney, spleen, and thymus are about 20–80% lower in the NHP compared to the newborn. Conversely, the masses of esophagus, heart, large intestine (LI) wall, salivary glands, small intestine (SI) wall, skeleton, stomach wall, tongue, ovaries, urinary bladder's wall, and uterus are 80–3000% higher in the NHP compared to the newborn. More detailed segmentation of the skeleton region of the NHP phantom is currently being carried out and new dosimetry results for substructures of skeleton system will become available soon.

3.B. AFs and SAFs

For all identified organs and tissues, results of radiation transport simulations were used to calculate AFs and SAFs for monoenergetic photons and electrons in the NHP phantom. Table S1 summarizes the SAFs for 31 photon source organs/tissues and 31 target tissues at 20 energy data points whereas Table S2 presents the SAFs for the same organs/tissues for electron sources at 13 energy data points. The wall and content uptakes of radiation in alimentary tract organs (e.g., stomach, LI and SI contents and walls) were independently considered in the dosimetric results.

Figure 3 shows the self-absorbed fractions of photons and electrons for the skin, brain, eye lens, kidney, liver, lung, skeleton, spleen, thyroid gland, ovaries, and uterus. The photon and electron AFs decrease with particle energy. For photons, the skeleton shows the highest self-absorbed fractions owing to its high density while the eye lens yields the lowest self-absorbed fraction values because of its small volume. Figure 4 shows the cross-absorbed fractions for the kidney irradiating surrounding organs. The photon cross-absorbed

AF curves follow a sharp increase until they reach a local maximum at 0.03 MeV. After these maximum values, the lines follow a gradual reduction, indicating that raising photon energy facilitates the escape of recoil electrons and scattered photons from the target organ. The electron cross-absorbed fraction curves increase with energy. Figure 5 shows the self-absorbed SAFs for photon and electron sources in major organs. All SAF curves decrease with increase particle energy. The eye lens presents the highest self-absorbed SAF owing to its small mass. Conversely, the skin displays the lowest self-absorbed SAF values because it has the biggest tissue mass, and its position and thickness facilitate the escape of radiation.

Figure 6 compares the self-absorbed SAF and cross-absorbed SAF between the newborn phantom and the NHP

TABLE II. Comparison between organ masses of the rhesus monkey phantom and the human newborn model

Organs	Organ mass (g)	
	Rhesus monkey	Newborn
Residual tissue ^a	2070.1	–
Skin	457	115.3
Adrenals	1.4	5.9
Bladder wall	3	3.9
Bladder content	1.8	–
Brain	73	315.4
Breasts	1.6	0.08
Esophagus	7.1	2
Eye balls	7.4	6
Eye lens	0.5	0.13
Gall Bladder	0.7	0.5
Heart	44.4	19.7
Kidney	19.1	24.7
Large intestine wall	42.8	11.1
Large intestine content	32.2	–
Liver	118.1	128.7
Lung	57.2	58.9
Pancreas	7.9	5.9
Salivary glands	26.8	3.5
Small intestine wall	125	29.1
Small intestine content	87.5	–
Skeleton	748.4	181.5
Spinal cord	10.4	6.5
Spleen	3.7	9.4
Stomach wall	221.8	6.9
Stomach content	106.1	–
Thymus	3.2	12.8
Thyroid	1.5	1.3
Tongue	12.9	3.5
Ovaries	0.9	0.3
Uterus	7	3.9
Total Body	4300	3317

^aNon-identified regions, such as muscles, connective tissues, blood vessels, and adipose tissues, were assigned to a single region, referred to as residual tissues.

phantom. Considerable differences were observed in both self-absorbed dose and cross-absorbed doses for some organs. The self-absorbed SAF of the uterus in the NHP phantom was 40–50% lower than the newborn model. Ratios of the self-absorbed $\text{SAF}_{(\text{stomach wall}) \text{ Monkey}}$ to $\text{SAF}_{(\text{stomach wall}) \text{ Newborn}}$ ranged from 0.06 at 10 keV to 0.29 at 3 MeV for photons while the ratios of self-absorbed $\text{SAF}_{(\text{brain}) \text{ Monkey}}$ to $\text{SAF}_{(\text{brain}) \text{ Newborn}}$ ranged from 2.39 at 50 keV to 4.19 at 10 keV for photons. The ratios of cross-absorbed $\text{SAF}_{(\text{liver} \rightarrow \text{kidney}) \text{ Monkey}}$ to $\text{SAF}_{(\text{liver} \rightarrow \text{kidney}) \text{ Newborn}}$ ranged from 0.78 at 50 keV to 5.78 at 10 keV for photons. Figure 7 compares the self-absorbed and cross-absorbed SAFs (liver as source organ) between the 1-year-old model and the NHP model. The ratios of the self-absorbed $\text{SAF}_{(\text{thymus}) \text{ Monkey}}$ to $\text{SAF}_{(\text{thymus}) \text{ 1-yr-old}}$ ranged from 4.26 at 2 MeV to 8.46 at 10 keV for photons while the ratios of self-absorbed $\text{SAF}_{(\text{uterus}) \text{ Monkey}}$ to $\text{SAF}_{(\text{uterus}) \text{ 1-yr-old}}$ ranged from 0.23 at 10 keV to 0.36 at 2 MeV for photons.

3.C. S-values

Table III compares the self-absorbed S-values for ^{131}I in the NHP phantom and published results for the newborn and

1-year-old female phantoms. S-values of the liver, lung, and thyroid in the NHP phantom are close to those of the newborn model (absolute differences are less than 8%) while the S-value of the ovaries in the NHP phantom is close to that of the 1-yr-old female (absolute difference of 7%). S-values of the adrenals, brain, kidneys, spleen, and thymus in the NHP phantom are appreciably larger than their human model counterparts while the S-values of the esophagus and uterus of the NHP phantom are substantially lower than those of human phantoms.

4. DISCUSSION

Accurate dosimetry calculations to various species used in preclinical research are important for optimizing the dose regimes for various radiopharmaceuticals and to investigate the collective absorbed dose and radiation risks associated with diagnostic imaging and radionuclide therapy procedures. For computational dosimetry, the use of NHP computational phantoms provides improved anatomical realism over surrogate human phantoms. With the use of computational NHP phantoms, it is possible to estimate organ absorbed doses, the quantity of interest, whereas previous

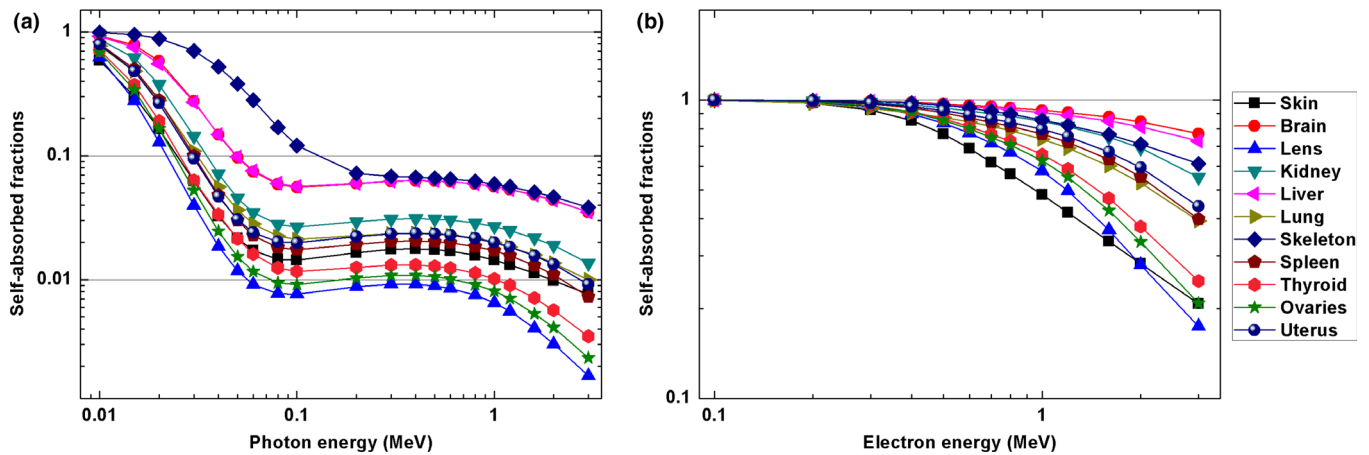


FIG. 3. Self-absorbed fractions for (a) photons and (b) electrons [Color figure can be viewed at wileyonlinelibrary.com]

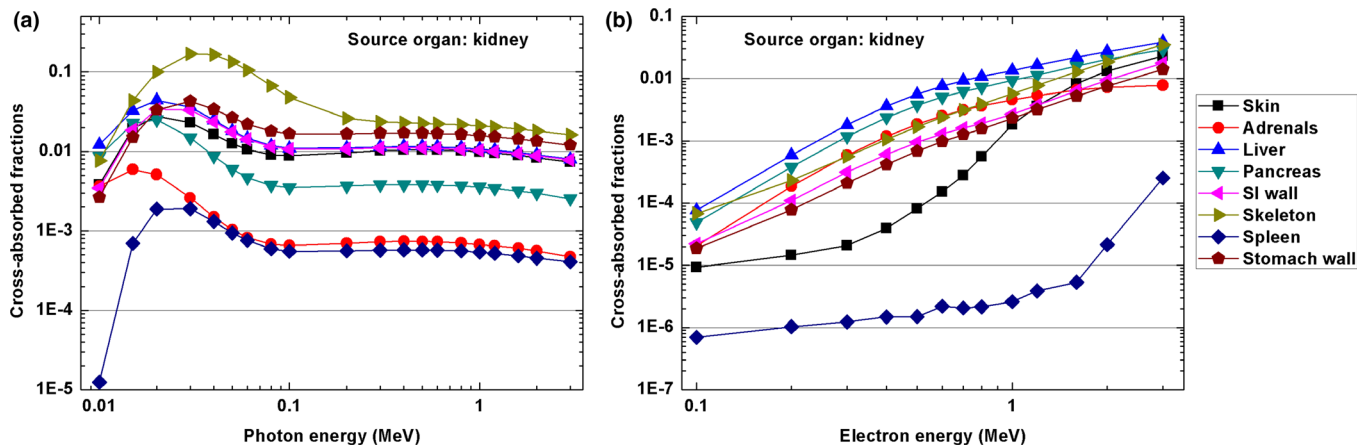


FIG. 4. Cross-absorbed fractions for (a) photons and (b) electrons for the kidney irradiating surrounding organs [Color figure can be viewed at wileyonlinelibrary.com]

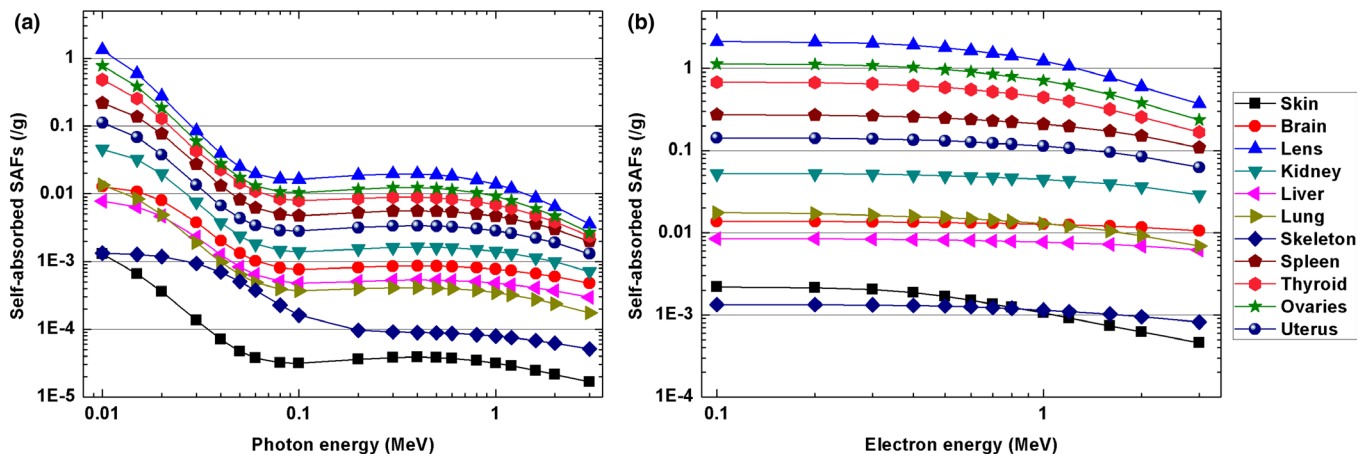


FIG. 5. Self-absorbed specific absorbed fractions for (a) photons and (b) electrons for major organs [Color figure can be viewed at wileyonlinelibrary.com]

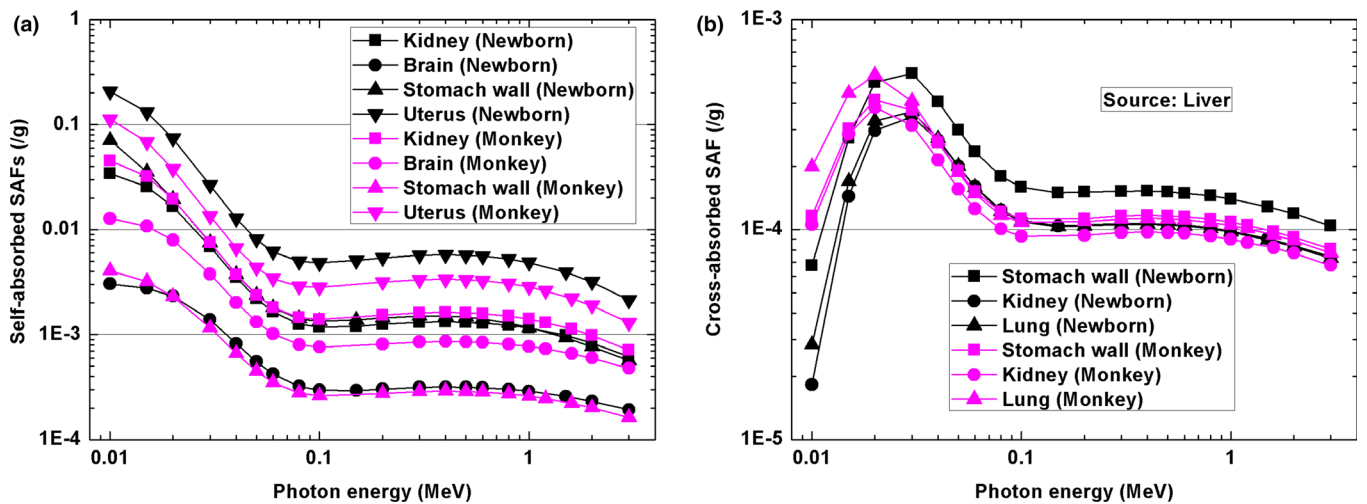


FIG. 6. Comparisons of (a) self-absorbed specific absorbed fractions (SAFs) and (b) cross-absorbed SAFs for selected organs between the monkey phantom and the newborn phantom 13 with similar total body weight [Color figure can be viewed at wileyonlinelibrary.com]

studies of external irradiation in ARS research relied on entrance surface dose measurements. In this work, we developed the first NHP computational model which may help improving dosimetry for nuclear medicine studies of radiopharmaceuticals and organ dose calculations for NHPs in radiation therapy research and ARS studies. Furthermore, dosimetric quantities, including AFs and SAFs for monoenergetic photons and electrons, were also systematically reported for internal radiation dosimetry. Of importance to AF and SAF estimations are the masses and 3D shapes of source and target organs, which might vary significantly between different computational models. We compared the dose estimates between the NHP phantom, ICRP reference newborn phantom, and 1-yr-old female phantom. Although the total body mass of the NHP phantom is close to the newborn, significant differences were observed between the two models for SAFs. The self-absorbed SAFs of the uterus and stomach wall in the NHP phantom are significantly lower than for the newborn phantom, whereas the self-absorbed SAF of the brain is considerably higher in the NHP

phantom. The body length of the NHP phantom and the 1-yr-old female are almost similar; however, the SAFs are considerably different between the two models for some organs. The results shown in Fig. 7 for photon sources in the kidney, liver, lung, spleen, and thymus indicate substantially higher values of self-absorbed SAFs per photon emission in the NHP phantom compared to the 1-yr-old female phantom, whereas $\text{SAF}_{(\text{uterus}) \text{ Monkey}}$ is significantly lower than $\text{SAF}_{(\text{uterus}) \text{ 1-yr-old}}$.

NHPs are often used to study the pharmacokinetics in pre-clinical studies to estimate the radiation dose in the human body;²⁵ however, radiation dosimetry calculations for NHPs are rarely done owing to the lack of a realistic NHP computational model. The reported NHP model provides a reliable model for radiation dosimetry studies. However, in preclinical research, the anatomy of NHPs may vary along different weights, heights, and age, and as such, more studies on the effect of anatomy variations on NHP radiation dosimetry may be needed. Another limitation of this work is the homogeneous skeleton where the density of cortical bone is used as

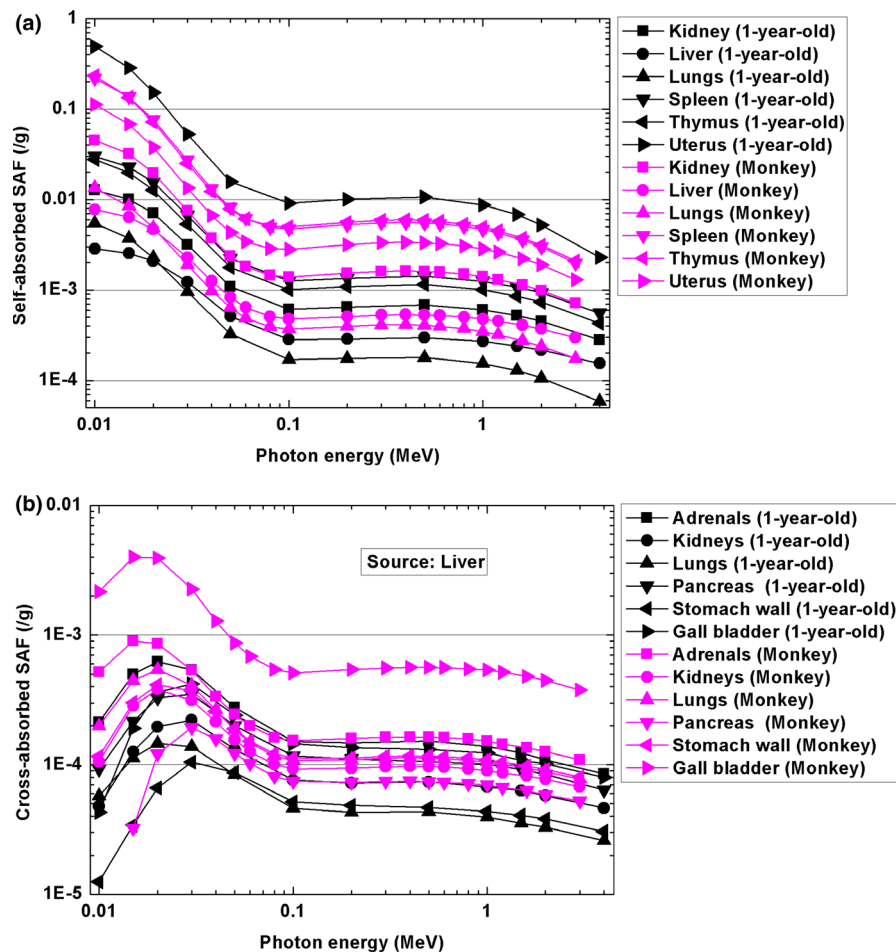


FIG. 7. Comparisons of (a) self-absorbed specific absorbed fractions (SAFs) and (b) cross-absorbed SAFs (liver as source organ) for selected organs between the monkey phantom and the 1-yr-old phantom 14 with similar body length [Color figure can be viewed at wileyonlinelibrary.com]

surrogate for density of all bony structures. This assumption may result in overestimation of absorbed fractions for the skeleton in the NHP model.

The AF and SAF of photons and electrons were used to calculate the S-values of ^{131}I in the NHP phantom. For radionuclide sources, although the total body mass of the NHP phantom is between the newborn and 1-yr-old models, the self-absorbed S-values to the adrenals, brain, kidneys, spleen, and thymus in the NHP phantom are much higher than those observed in either the newborn or 1-yr-old phantom. Differences in AFs, SAFs, and S-values can be attributed to several parameters, including the masses and shapes of the source and target organs, orientations, and positions with respect to one another in a given computational model. For instance, the mass of the lung, liver, and thyroid in the NHP phantom are similar to those in the newborn phantom. Therefore, differences in S-values for these organs between the two models are <8%. The dosimetry database provided in the Supplemental materials can be exploited for the calculation of S-values and absorbed doses for various radionuclides and radiotracers in preclinical studies involving the use of NHP models.

TABLE III. Comparison of self-absorbed S-values for ^{131}I between the monkey phantom, newborn phantom,¹³ and 1-yr-old pediatric phantom.²⁶

Organ	Self-absorbed S-values from ^{131}I ($\times 10^{-03}$ mGy/MBq/s)		
	Monkey	Newborn	1-yr-old
Adrenals	22.64	5.17	7.72
Brain	0.47	0.12	0.04
Esophagus	4.43	14.51	6.11
Kidney	1.70	1.24	0.47
Liver	0.29	0.27	0.11
Lungs	0.55	0.54	0.21
Ovaries	35.13	94.88	37.63
Pancreas	4.00	5.21	1.62
Spleen	8.65	3.35	1.13
Thymus	9.84	2.51	1.07
Thyroid	21.16	22.62	16.66
Uterus	4.55	7.89	20.46

5. CONCLUSIONS

We developed the first NHP voxel-based and NURBS-based computational phantoms based on tomographic images

and color cryosection images. The AFs and SAFs of monoenergetic photons and electrons were generated for radiation dose calculations in preclinical research where the use of NHP subjects offers significant advantages over other laboratory animals. The NHP computational model described in this work can solve the problems arising from the use of human phantoms in research studies involving the use of NHPs. Future studies will focus on enhancing the skeleton system by adding detailed structures of cortical bone, trabecular bone, RBM, and YBM to the NHP phantom. The NHP dosimetry database can be exploited for the assessment of radiation dose to NHPs from novel radiopharmaceuticals. The NHP model can also be used to generate a large number of NHP models by varying the anthropometric characteristics of the developed anchor model for personalized dosimetry calculations.

FUNDING

This study was supported by a start-up grant from Fudan University to T.X., the Swiss National Science Foundation under grant SNFN 320030_176052, Qatar national research fund (NPRP10-0126-170263) and the National Key R&D Program of China (Grant no. 2016YFF0200804).

CONFLICT OF INTEREST

All authors declare that they have no conflict of interest.

ETHICAL APPROVAL

All applicable international, national, and/or institutional guidelines for the care and use of animals were followed. The study protocol was reviewed and approved by the Institutional Review Board (IRB) of National Primate Research Center of Korea Research Institute of Bioscience and Biotechnology (IRB No. KRIBB-AEC-18087). Written informed consent was not required for this study.

^{a)} Author to whom correspondence should be addressed. Electronic mail: tianwuxie@fudan.edu.cn; Telephone: +86 21 6404 8363; Fax: +86 21 6404 8363.

REFERENCES

- Tuveson D, Hanahan D. Translational medicine: cancer lessons from mice to humans. *Nature*. 2011;471:316–317.
- Zaidi H, ed. *Molecular Imaging of Small Animals: Instrumentation and Applications*. New York: Springer; 2014.
- Singh VK, Olabisi AO. Nonhuman primates as models for the discovery and development of radiation countermeasures. *Expert Opin Drug Discov*. 2017;12:695–709.
- Suit H, Goldberg S, Niemierko A, et al. Secondary carcinogenesis in patients treated with radiation: a review of data on radiation-induced cancers in human, non-human primate, canine and rodent subjects. *Radiat Res*. 2007;167:12–42.
- Farese AM, Cohen MV, Katz BP, et al. A nonhuman primate model of the hematopoietic acute radiation syndrome plus medical management. *Health Phys*. 2012;103:367–382.
- Bujold K, Hauer-Jensen M, Donini O, et al. Citrulline as a biomarker for gastrointestinal-acute radiation syndrome: species differences and experimental condition effects. *Radiat Res*. 2016;186:71–78.
- Xie T, Zaidi H. Development of computational small animal models and their applications in preclinical imaging and therapy research. *Med Phys*. 2016;43:111–131.
- Zaidi H. *Computational Anatomical Animal Models: Methodological developments and research applications*. Bristol, UK: IOP Publishing; 2018.
- Kasten BB, Azure MT, Schoeb TR, Fisher DR, Zinn KR. Imaging, biodistribution, and toxicology evaluation of (212)Pb-TCMC-trastuzumab in nonhuman primates. *Nucl Med Biol*. 2016;43:391–396.
- Jia B, Liu Z, Zhu Z, et al. Blood clearance kinetics, biodistribution, and radiation dosimetry of a kit-formulated integrin alphavbeta3-selective radiotracer 99mTc-3PRGD 2 in non-human primates. *Mol Imaging Biol*. 2011;13:730–736.
- Nishii R, Tong W, Wendt R 3rd, et al. Pharmacokinetics, metabolism, biodistribution, radiation dosimetry, and toxicology of (18)F-Fluoroacetate ((18)F-FACE) in non-human primates. *Mol Imaging Biol*. 2012;14:213–224.
- Antenor-Dorsey JA, Laforest R, Moerlein SM, Videen TO, Perlmutter JS. Radiation dosimetry of N-([11C]methyl)benperidol as determined by whole-body PET imaging of primates. *Eur J Nucl Med Mol Imaging*. 2008;35:771–778.
- Wayson M, Lee C, Sgouros G, Treves ST, Frey E, Bolch WE. Internal photon and electron dosimetry of the newborn patient—a hybrid computational phantom study. *Phys Med Biol*. 2012;57:1433–1457.
- Stabin MG, Emmons MA, Segars WP, Fernald MJ. Realistic reference adult and paediatric phantom series for internal and external dosimetry. *Radiat Prot Dosimetry*. 2012;149:56–59.
- Chung BS, Jeon CY, Huh JW, et al. Rise of the visible monkey: sectioned images of rhesus monkey. *J Korean Med Sci*. 2019;34:e66.
- Schroeder W, Avila L, Hoffman W. Visualizing with VTK: a tutorial. *IEEE Comput Graphics Appl*. 2000;20:20–27.
- Pelowitz DB. *MCNPX User's Manual Version 2.5.0*. Los Alamos, NM: Los Alamos National Laboratory; 2005. LA-CP-05-0369.
- ICRP. Publication 89: basic anatomical and physiological data for use in radiological protection: reference values. *Ann ICRP*. 2002;32:1–277.
- Sechopoulos I, Rogers DW, Bazalova-Carter M, et al. RECORDS: improved reporting of monte Carlo RaDiation transport studies: report of the AAPM Research Committee Task Group 268. *Med Phys*. 2018;45:e1–e5.
- Bolch WE, Eckerman KF, Sgouros G, Thomas SRMIRD. Pamphlet No. 21: a generalized schema for radiopharmaceutical dosimetry – standardization of nomenclature. *J Nucl Med*. 2009;50:477–484.
- Xie T, Kuster N, Zaidi H. Effects of body habitus on internal radiation dose calculations using the 5-year-old anthropomorphic male models. *Phys Med Biol*. 2017;62:6185–6206.
- Seidlin SM, Marinelli LD, Oshry E. Radioactive iodine therapy; effect on functioning metastases of adenocarcinoma of the thyroid. *J Am Med Assoc*. 1946;132:838–847.
- Nemecek ER, Matthews DC. Use of radiolabeled antibodies in the treatment of childhood acute leukemia. *Pediatr Transplant*. 2003;7:89–94.
- RADAR. Decay data. Available on <http://www.doseinfo-radar.com/RADARDecay.html> accessed March 2019.
- Stabin MG, Sparks RB, Crowe E. OLINDA/EXM: the second-generation personal computer software for internal dose assessment in nuclear medicine. *J Nucl Med*. 2005;46:1023–1027.
- Stabin MG, Xu XG, Emmons MA, Segars WP, Shi C, Fernald MJ. RADAR reference adult, pediatric, and pregnant female phantom series for internal and external dosimetry. *J Nucl Med*. 2012;53:1807–1813.

SUPPORTING INFORMATION

Additional supporting information may be found online in the Supporting Information section at the end of the article.

Table S1. Licensure for MCNP Packages used in this work.

Table S2. Licensure for MCNP Medias used in this work.